Multiphysics modelling of the separation of suspended particles via frequency ramping of ultrasonic standing waves

Francisco J. Trujillo [a,*], Sebastian Eberhardt [b], Dirk Möller [c], Jurg Dual [c], Kai Knoerzer [b]

[a] School of Chemical Engineering, University of New South Wales, Sydney, NSW 2052, Australia
[b] CSIRO Food and Nutritional Sciences, Werribee, VIC, Australia
[c] Institute of Mechanical Systems – Centre of Mechanics, ETH Zurich, Tannenstrasse 3, 8292 Zurich, Switzerland

ABSTRACT

A model was developed to determine the local changes of concentration of particles and the formations of bands induced by a standing acoustic wave field subjected to a sawtooth frequency ramping pattern. The mass transport equation was modified to incorporate the effect of acoustic forces on the concentration of particles. This was achieved by balancing the forces acting on particles. The frequency ramping was implemented as a parametric sweep for the time harmonic frequency response in time steps of 0.1 s. The physics phenomena of piezoelectricity, acoustic fields and diffusion of particles were coupled and solved in COMSOL Multiphysics™ (COMSOL AB, Stockholm, Sweden) following a three step approach. The first step solves the governing partial differential equations describing the acoustic field by assuming that the pressure field achieves a pseudo steady state. In the second step, the acoustic radiation force is calculated from the pressure field. The final step allows calculating the locally changing concentration of particles as a function of time by solving the modified equation of particle transport. The diffusivity was calculated as function of concentration following the Garg and Ruthven [1] equation which describes the steep increase of diffusivity when the concentration approaches saturation. However, it was found that this steep increase creates numerical instabilities at high voltages (in the piezoelectricity equations) and high initial particle concentration. The model was simplified to a pseudo one-dimensional case due to computation power limitations. The predicted particle distribution calculated with the model is in good agreement with the experimental data as it follows accurately the movement of the bands in the centre of the chamber.

Crown Copyright © 2012 Published by Elsevier B.V. All rights reserved.

1. Introduction

The separation of suspended particles via acoustic radiation forces has found several applications in medical and life sciences fields where microchip configurations have been developed to move, concentrate and manipulate biological cells, micrometre sized solid particles and droplets suspended in immiscible fluid [2]. The primary acoustic force translates particles to either the node or antinode of the standing wave. This force decreases with particle size but increases with frequency. Hence, in order to separate particles with sizes of only a few micrometres, frequencies higher than 1 MHz are preferred to achieve sufficient separation. This principle has been successfully implemented in microchannels, where the acoustic resonator can be tuned to match a half wavelength (less than a millimetre for frequencies higher than 1 MHz). This, followed by advances in silicon/glass micro fabrication technologies, while taking advantage of the laminar flow developed on micro-channels, has opened the door to develop lab-on-a-chip technologies, where both acoustic trapping and continuous flow separation has merged, showing great potential to develop applications such as acoustic cytometers [3], cell sorting [4], droplet sorting [5] and ultrasonic levitation [6], among others.

Although research on larger scale application is limited, studies have been conducted on emulsion splitting, i.e., for recovering crude oil from emulsions in oilfields [7], for recycling wastewater and separating valuable components from wool scouring [8], for biodiesel production [9] and in food processing to enhance creaming of milk fat [10]. While the primary acoustic force traps the particle within the standing wave, additional forces such as secondary acoustic forces, gravity and drag force are utilised to move particles to desired locations [11]. For instance, acoustically enhanced sedimentation or flocculation use the standing wave to trap particles on planes perpendicular to the direction of sound propagation, where secondary acoustic forces agglomerate the particles within the bands. Then, after turning the acoustic field off, the larger agglomerates sediment or float due to gravitational/buoyancy forces, provided that the agglomerates are stable after the

* Corresponding author.
E-mail address: Francisco.Trujillo@unsw.edu.au (F.J. Trujillo).

Nomenclature

Latin symbols

a_0	acceleration at the boundary (m s^{-2})
c	speed of sound (m s^{-1})
c_0	standard concentration defined as 1 (mol l^{-1})
c_l	speed of sound of the liquid (m s^{-1})
c_p	concentration of particles (mol m^{-3})
c_s	speed of sound of the solid particles (m s^{-1})
c_{sat}	concentration of particles at saturation (mol m^{-3})
C_D	drag coefficient (kg s^{-1})
D	diffusion coefficient (m^2 s^{-1})
D_0	diffusion coefficient at low concentration (m^2 s^{-1})
f	frequency (s^{-1})
F_{Drag}	drag force (N/mol^{-1})
F_μ	force due to the gradient of chemical potential (N/mol^{-1})
F_{Rad}	primary acoustic radiation force (N/mol^{-1})
h	mesh element size (m)
i	imaginary unit number
k_b	Boltzmann constant = 1.380 6 × 10^{-23} (J K^{-1})
m_p	mass of a single particle (kg)
$\dot{m}_p$	mass flux of particles (kg m^{-2} s^{-1})
n	unit normal vector
N_A	Avogadro constant = 6.022 × 10^{23} (particles mol^{-1})
$\dot{N}_j$	flux of species (mol m^{-2} s^{-1})
$\dot{N}_p$	molar flux of particles (mol m^{-2} s^{-1})
p	fluid pressure (Pa)
$\langle p^2 \rangle$	mean square pressure fluctuation of the sound field (Pa^2)
P	Amplitude of the acoustic pressure (Pa)
Pe	Peclet number
r	radius of particles (m)
R	universal gas constant = 8.314 (J mol^{-1} K^{-1})
t	time (s)
T	temperature (K)
U_{Rad}	acoustic force potential (kg m^2 s^{-2})
$\langle v^2 \rangle$	mean square velocity fluctuation of the sound field (m^2 s^{-2})
v_p	velocity of the particle (m s^{-1})
x_p	mass fraction of particles

Greek symbols

α_{Pe}	convective term (m s^{-1})
η	viscosity (Pa s)
κ	compressibility $\kappa = 1/\rho c^2$ (Pa^{-1})
μ_0	chemical potential at standard conditions (J mol^{-1})
μ_p	chemical potential of particles (J mol^{-1})
ρ	density (kg m^{-3})
ρ_l	liquid density (kg m^{-3})
ρ_s	solid particle density (kg m^{-3})
ρ_r	total density (kg m^{-3})
σ	stress tensor (Pa)
Φ_Y	acoustic contrast factor
$\omega = 2\pi f$	angular frequency (rad s^{-1})

Operators

<>	time average
∇	nabla operator
∂	partial differential

sonication period and do not redisperse [11]. Ramping the frequency in a sawtooth pattern [12], which will be studied in this paper, has also been used to displace particles towards the reflector or the acoustic source, depending on the acoustic contrast factor and whether the ramping is conducted from a lower to a higher frequency or vice versa. For instance, particles with a positive contrast factor in a ramping system from lower to higher frequency will be displaced towards the reflector, while particles with a negative contrast factor will be displaced towards the acoustic source under the same ramping pattern.

Parallel to designing lab-on-a-chip applications, there has been significant advances into developing mathematical models to describe the resonance modes on microchips, aiming to predict the acoustic force and the pressure amplitude acting on suspended particles [13]. Building an efficient resonator is a complex task as fine tuning is required to design the resonator in a way that optimal acoustic coupling and maximum energy transmission into the fluid is achieved [14]. Initial models such as the layered resonator uses an equivalent circuit transducer model coupled with the acoustic impedance transfer relationship to model acoustic cells [15]. This model shows the effect of resonances on cell layers and its effect on pressure distribution as a function of frequency. More advanced modelling efforts solve the Helmholtz wave equation for the pressure amplitude of the wave and potential flow for the velocity amplitude of the acoustic oscillation [13,16]. Once the pressure and velocity amplitudes of the acoustic wave has been determined, the acoustic force acting on particles can be predicted by solving Gor'kov's equation [17], which describes the force potential exerted on particles by an acoustic field. After modelling the acoustic field and calculating Gor'kov's potential, the path of single particle can be modelled by balancing the forces acting on that particle; namely, acoustic force, drag and buoyancy [18], while

coupling it with the fluid velocity profile predicted by computational fluid dynamics (CFD). By modelling a series of particles at the channel inlet and using the resulting particle coordinates, Townsend et al. [18] estimated the change of concentration across the channel. While this modelling approach may be sufficient for designing and modelling microchannels, it is not suitable for larger scale systems where more pronounced gradients on the acoustic field and particle concentration are present. Hence, in this work we are proposing to model the change of concentration of particles by solving the mass transport equation, which will be modified to account for the effect of the acoustic field. This way, the concentration of particles will be described by a diffusion model instead of by tracking the movement of single particles.

2. Mathematical model

2.1. Governing equations for the transport of concentrated species

2.1.1. Balance of forces on particles to determine the mass flux of particles

A group of particles in a stagnant liquid will randomly move (Brownian motion) or diffuse following the gradient of the chemical potential μ_p. The effect of the gradient of chemical potential on particles can be represented by the force F_μ even though the Brownian motion is due to the random movement of particles. When those particles are subjected to an ultrasonic standing wave, the primary acoustic force F_{Rad} will move those particles towards the pressure nodes or antinodes for materials exhibiting a positive contrast factor (explained on Section 2.7) or a negative contrast factor, respectively. Particles moving in a viscous liquid will experience the Stokes drag force F_{Drag}. For small particles it is reason-

able to neglect the particles' inertia and to assume that they are always moving in a local steady state [19]. Hence, the forces acting on the particle are balanced:

$$F_\mu + F_{Rad} + F_{Drag} = 0 \tag{1}$$

For a spherical particle with radius r, moving at a velocity v_p through a liquid with viscosity η, the Stokes drag force F_{Drag} can be expressed as:

$$F_{Drag} = -6\pi\eta r v_p \tag{2}$$

Eq. (2) is valid for a single particle. By assuming that particles are not interfering with each other, the equation above can be multiplied by the Avogadro constant N_A to estimate the drag of one mole, i.e., 6.022×10^{23}, of particles:

$$F_{Drag} = -6\pi\eta r v_p N_A \tag{3}$$

The acoustic radiation force can be obtained from the acoustic force potential as [13]:

$$F_{Rad} = -\nabla U_{Rad} \tag{4}$$

where the acoustic force potential has been derived by Gor'kov [20] as:

$$U_{Rad} = \frac{4\pi}{3} r^3 \left[f_1 \frac{1}{2\rho_l c_l^2} \langle p^2 \rangle - f_2 \frac{3}{4} \rho_l \langle v^2 \rangle \right] \tag{5}$$

$$f_1 = 1 - \frac{\kappa_s}{\kappa_l} \tag{6}$$

$$f_2 = \frac{2(\rho_s - \rho_l)}{(2\rho_s + \rho_l)} \tag{7}$$

The terms $\langle p^2 \rangle$ and $\langle v^2 \rangle$ are the mean square pressure amplitude fluctuation of the sound field and of the particle velocity, respectively, and can be determined by solving the Helmholtz equation. κ and ρ are compressibility and density while the subscripts l and s stand for "liquid" and "solid particle", respectively. Eq. (4) describes the acoustic force potential on a single particle. Again, by assuming that particles do not interfere with each other and neglecting multiple wave scattering between particles, Eq. (4) can be multiplied by the Avogadro constant N_A to account for the radiation force per mole of particles:

$$F_{Rad} = -N_A \nabla U_{Rad} \tag{8}$$

F_μ is given by:

$$F_\mu = -\nabla \mu_p \tag{9}$$

where μ_p is the chemical potential, which for small concentration of particles can be expressed as:

$$\mu_p = \mu_0 + RT \ln\left(\frac{c_p}{c_0}\right) \tag{10}$$

where R is the universal gas constant ($8.314\, J\, mol^{-1}\, K^{-1}$), T is the temperature, c_p is the concentration of particles, μ_0 is the chemical potential at standard conditions and c_0 the standard concentration defined as 1 mol/l. The gradient of the chemical potential is:

$$\nabla\mu_p = \frac{RT}{c_p} \nabla c_p \tag{11}$$

Combining Eqs. (1), (3), (8), and (11), while applying the Einstein–Stokes equation

$$6\pi\eta r = \frac{k_b T}{D} \tag{12}$$

and introducing the Boltzmann constant $k_b = \frac{R}{N_A}$ leads to:

$$-D\nabla c_p - \frac{c_p}{C_D} \nabla U_{Rad} = c_p v_p \tag{13}$$

where D is the diffusion coefficient, and $C_D = 6\pi\eta r$ is the drag coefficient of a single particle. The term $c_p v_p$ is the molar flux of particles $\dot{N}_p$ with respect to a fixed spatial coordinate system and therefore:

$$\dot{N}_p = c_p v_p = -D\nabla c_p - \frac{c_p}{C_D} \nabla U_{Rad} \tag{14}$$

The total density of the fluid ρ_T, including the particles was calculated as:

$$\rho_T = x_p \rho_s + (1 - x_p)\rho_l \tag{15}$$

where x_p is the mass fraction of particles. ρ_s = 1050 kg m^{-3} and ρ_l = 998 kg m^{-3} are the density of the particles and liquid, respectively. Because ρ_s and ρ_l are similar, the model can be simplified by assuming that the total density is constant. In that case, the continuity equation shows that the total velocity v is zero:

$$\begin{aligned} &\frac{\partial \rho_t}{\partial t} + \nabla \cdot (\rho_t v) = 0 \\ &\nabla \cdot (v) = 0 \\ &\nabla \cdot (v_p + v_l) = 0 \end{aligned} \tag{16}$$

This means that a movement of particles at a certain velocity and carrying a certain mass will be balanced by a movement of water carrying the same mass at the same velocity but in the opposite direction. The molar concentration of particles can be expressed as:

$$c_p = \frac{x_p \rho_T}{m_p N_A} \tag{17}$$

where m_p is the mass of a single particle. The mass flux of particles $\dot{m}_p$ can be obtained by multiplying the molar flux of particles by $m_p N_A$:

$$\dot{m}_p = m_p N_A \dot{N}_p \tag{18}$$

Replacing Eqs. (14) and (17) into Eq. (18) leads to:

$$\dot{m}_p = -D\nabla(x_p \rho_T) - \frac{\nabla U_{Rad}}{C_D}(x_p \rho_T) \tag{19}$$

In the next section, the mass flux of particles $\dot{m}_p$ is incorporated into the total mass balance equation.

2.1.2. Total mass balance of particles

The time dependent mass balance of particles can be expressed as:

$$\frac{\partial}{\partial t}(x_p \rho_T) + \nabla(\dot{m}_p) = 0 \tag{20}$$

Inserting the mass flux of particles (c.f., Eq. (19)) in Eq. (20) leads to the final equation of the mass balance of particles:

$$\underbrace{\frac{\partial}{\partial t}(x_p \rho_T)}_{\text{Accumulation}} + \nabla \cdot \left(\underbrace{-D\nabla(x_p \rho_T)}_{\text{Diffusion}} - \underbrace{\frac{\nabla U_{Rad}}{C_D}(x_p \rho_T)}_{\text{Convection}} \right) = 0 \tag{21}$$

The terms of the equation can be compared with a general transport equation by identifying the accumulation, diffusion and convective terms. The diffusivity (or diffusion coefficient) for low concentrations of particles can be calculated according to the Einstein–Stokes equation:

$$D_o = \frac{k_b T}{6\pi\eta r} \tag{22}$$

However, this equation only accounts for the diffusion of spherical particles at low concentrations. Because the acoustic force rapidly focuses particles at the nodes (or antinodes), neglecting the effect of the concentration on diffusivity can lead to unrealistically

high concentrations during modelling. To correct this, the effect of concentration was incorporated following the equation proposed by Garg and Ruthven [1]:

$$D = \frac{D_o}{\left(1 - \frac{c_p}{c_{sat}}\right)} \quad (23)$$

where c_{sat} is the concentration at saturation and D_o is the limiting diffusivity as $c_p \rightarrow 0$. According to this equation, the diffusivity will reach infinity at the saturation point which is the maximum concentration of the particles tightly packed. The equation was developed to account for the concentration dependence of diffusivity on zeolitic sorption curves. It reflects the fact that the rate of absorption and desorption depends on the availability of free spaces on the zeolite. It seems valid to use the pore diffusion approach when considering the band of particles as a porous media, where the amount of particles entering and leaving the band depends on the already occupied space within the band. If the band is saturated with particles tightly packed the diffusion term in Eq. (21) will balance the convective term. In other words, the concentration of particles on the band cannot be higher than the saturation concentration regardless of the extent of the acoustic force, which is a sound representation of the formation of bands.

2.2. Governing equations for the acoustic pressure and velocity field

The time independent form of the linear wave equation for harmonic waves can be represented by the Helmholtz wave equation for the pressure and the potential flow for the velocity:

$$\nabla^2 P - \frac{\omega^2}{c^2} P = 0 \quad (24)$$

$$v = -\frac{i}{\omega\rho} \nabla P \quad (25)$$

where c and ρ are the speed of sound and the density of the fluid, respectively, ω is the angular frequency and P is the amplitude of the acoustic pressure. Solving the Helmholtz equation allows to determine the mean square fluctuation of the acoustic pressure $<p^2>$ and the velocity $<v^2>$, which is needed to calculate the primary acoustic force via Gork'ov's potential (c.f., Eqs. (5)–(7)).

2.3. Geometrical configuration

Fig. 1 shows the experimental setup designed by Möller et al. [21] and Dual et al. [22]. They studied the effect of frequency ramping on the separation of Polystyrene particles suspended in water. The device is aligned horizontally on a plane perpendicular to the gravitational force. Experimental results were represented by
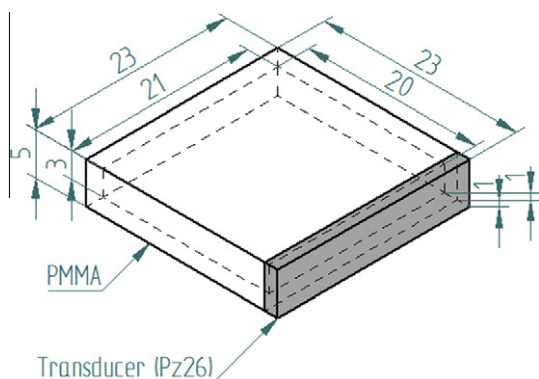

Fig. 1. Separation chamber with transducer (dimensions are given in mm).

digital images taken with an Olympus SZH microscope equipped with an Imperx IPX-2M30-L camera with a resolution of 1600×1200, showing the formations of bands for initial conditions, 40 and 120 s. Their data was used to validate the model presented in this paper. The setup consists of a 23 mm × 23 mm × 5 mm poly(methylmethacrylate) PMMA chamber with a wall thickness of 1 mm. A lead zirconate titanate ceramics transducer PZ26 was attached to one side of the wall as illustrated in Fig. 1. The separation chamber was filled with water and polystyrene particles through two 1 mm holes in opposing corners of the top cover. Due to the vibration of the transducer, a displacement of the adjacent PMMA leads to the propagation of an acoustic wave through the fluid and reflection on the opposite wall, resulting in the formation of standing waves within the fluid that can trap the particles in the pressure nodes. Hence, in order to concentrate the particles on one side of the chamber, the pressure nodes have to move, which was realised by implementing a so called sawtooth frequency sweep, where the frequency was increased linearly from 1.5 to 2.5 MHz for a period of 20 s. After that, the frequency drops back to 1.5 MHz and a new ramp is started. By continuously increasing the frequency during each ramp, new pressure nodes and antinodes are introduced into the system. The higher the frequency, the lower the wavelength; hence the number of nodes and antinodes increases with increasing frequency. The initial nodes are moved towards the reflector opening space for new nodes to be introduced in the vicinity of the transducer. As the acoustic force moves the particles towards the nodes of the wave, the particles are moved towards the reflector following the displacement of the bands.

As reported by Möller et al. [23] and Dual et al. [22] and earlier in this manuscript, the processing chamber was filled with a mixture of water and suspended polystyrene particles. After the chamber was filled and the particles were uniformly distributed in the suspension, the transducer was switched on at a peak to peak voltage setting of 10 V and an initial frequency of 1.5 MHz. Then, ramping was performed from 1.5 to 2.5 MHz for periods of 20 s, as described earlier. Ramps were repeated six times and photographs were taken at 0, 40 and 120 s. The photograph taken at time zero refers to the moment when the ramping has started, after the initial frequency of 1.5 MHz has been established forming an initial steady pattern of bands filled with particles. This means that at time zero, particles are already focused on the bands. Photographs at 40 and 120 s were taken at the beginning of the next sweeping cycle where the frequency is 1.5 MHz.

2.4. Model setup

The coupled phenomena of piezoelectricity, acoustic fields and diffusion of particles was modelled with COMSOL Multiphysics™ (COMSOL AB, Stockholm, Sweden) coupling the respective governing partial differential equations describing piezoelectricity, pressure acoustics and transport of species, as implemented in the software package. The frequency ramping was introduced as a parametric sweep for the time harmonic frequency response in time steps of 0.1 s, which is equivalent to frequency steps of 5 kHz from 1.5 to 2.5 MHz. The frequency as a function of time within a 20 s period is given by:

$$f[\text{kHz}] = \frac{t}{0.1\text{ s}} * 5\text{ kHz} + 1500\text{ kHz} \quad (26)$$

The solution is obtained, as mentioned earlier, in a three step approach. In the first step, the piezoelectricity, as well as the pressure acoustics components of the multiphysics scenario, was solved using a time harmonic frequency response (Helmholtz equation) for each frequency corresponding to a specific time step. The stationary prediction of the pressure amplitude can be justified by the high speed of sound, which rapidly achieves a pseudo-

steady state in the relatively small chamber configuration. In the second step, the stationary predictions of pressure and velocity are used to calculate the acoustic radiation force. In the third step, the acoustic force is used to solve the transient transport of particles (c.f., Eq. (21)) for a time step of 0.1 s. Intermediate time steps within the 0.1 s interval were automatically selected by the software package ensuring numerical stability to solve Eq. (21).

Solving the Helmholtz equation at a frequency of 2.5 MHz (wavelength of 0.5 mm) requires a mesh size of 0.05 mm to locate at least ten nodal points within a wavelength. However, the movement of particles occurs in a half wavelength distance, which is characterised by sharp concentration gradients and, therefore, a very fine mesh was required. Due to this, the model was solved pseudo one-dimensional, and the mesh size was fixed at 0.002 mm after conducting preliminary runs to confirm the mesh size independence of the simulation. The modelled geometry, depicted in Fig. 2, consists of the transducer with a thickness of 1 mm, the PMMA wall with a thickness of 1 mm, the separation chamber with a total length of 20 mm and another PMMA wall of 1 mm on the right. The numerical scheme of the utilised software package does not allow solving the piezoelectricity component on one-dimensional domains; this problem could be circumvented by constructing the geometry as a slim 2D strip with a height of 0.02 mm, where the selected top and bottom boundary conditions force the modelling to be one-dimensional; i.e., a pseudo one-dimensional modelling domain was realised.

The considered problem was discretised using the finite element method (FEM) and a mapped mesh consisting of 10,000 quadrilateral elements in x-direction and 10 quadrilateral elements in y-direction for the fluid domain. The transducer and PMMA walls were modelled with 90 quadrilateral elements for each section. The overall number of elements, therefore, sums up to 100,270. No further noticeable change in the model output could be observed by increasing the number of mesh elements. Computations were carried out on a Linux cluster system running Ubuntu 10.04. Four Intel® Xeon X5670 processors, each consisting of 6 cores (2.93 Ghz, 12 M Cache) and 94.6 GB RAM allowed for solving 1 s of ramping in approximately 1000 s. This lengthy solving process of the fully coupled scenario was caused by the automatic selection and adjustment of very small time steps, within the 0.1 s interval to ensure numerical stability when solving Eq. (21).

2.5. Boundary conditions

The boundaries are numbered in Fig. 2. A sinusoidal signal was applied to the electrode (boundary 1) with a maximum electrical potential of 7 V, whereas on the return electrode (boundary 2) a ground boundary condition (zero voltage) was implemented. A voltage of 7 V was selected as the model became instable for higher voltages. For boundaries 3 and 4 electrical insulation is assumed. To describe the coupling of the fluid domain with the linear elastic deformation of the PMMA a pressure boundary load was applied on the wall neighbouring the fluid domain (boundary 7 and 10):

$$\sigma \cdot n = -p \cdot n \tag{27}$$

where σ denotes the stress and p the fluid pressure. Boundaries 1, 3, 4, 5, 6, 11, 12, 13 were set to 'free', which means there are no loads or constraints acting on the boundary. The harmonic vibration of the PMMA sets the fluid in motion and generates an acoustic wave travelling through the fluid domain. To calculate the pressure wave, an acceleration boundary was applied on the fluid side of the PMMA walls to couple the vibration generated at the piezoelectric device with the fluid domain. The acceleration boundary (boundary 7 and 10) was defined by:

$$-n \cdot \left(-\frac{1}{\rho} (\nabla p) \right) = -n \cdot a_0 \tag{28}$$

Top and bottom of the geometry (boundaries 8 and 9) were simplified by using a sound hard boundary:

$$-n \cdot \left(-\frac{1}{\rho} (\nabla p) \right) = 0 \tag{29}$$

For the transport of particles, the conservation of mass is guaranteed by a no flux boundary (boundary 7, 8, 9, 10) around the fluid domain:

$$-n \cdot \dot{N}_j = 0 \tag{30}$$

2.6. Stabilisation techniques

Eq. (21) is a convection–diffusion transport equation which becomes unstable for:

$$Pe = \frac{\|\alpha_{Pe}\| h}{2D} > 1 \tag{31}$$

where h is the mesh element size, D the diffusivity and α_{Pe} is the convective term (right hand side term in Eq. (21)). A Péclet number greater than one indicates that convective flow dominates over diffusion. According to Eq. (31) stabilisation can be achieved by reducing the mesh size; however in practice this is not feasible due to computational limitations. For instance, in order to get $Pe < 1$ at 1.51 MHz, a mesh element size of 2e-11 m would be required, which is by far beyond the available computational power. Stabilisation was achieved with isotropic diffusion and streamline diffusion, which are stabilisation techniques implemented in the utilised software package COMSOL Multiphysics™. Isotropic diffusion adds a term to the convective coefficient of the transport equation to tune the solution and smooth instabilities. Streamline diffusion modifies the added term in a way that only adds artificial diffusion in the direction of the flow.

2.7. Material properties

As mentioned earlier in the manuscript, the density of the water and the polystyrene particles was set to 980 kg/m³ and 1050 kg/m³, respectively. The dynamic viscosity of water was set to $\eta = 10^{-3}$ Pa s, which represents the value for pure water at 25 °C. The
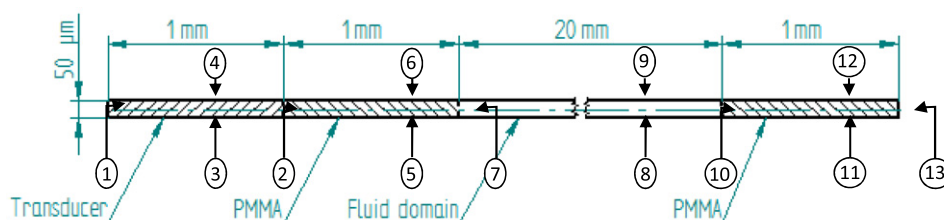

Fig. 2. Modelled one-dimensional geometry including, the transducer, the PMMA walls and the separation domain. The numbers are referring to the specific boundaries.

polystyrene particles are assumed to be spheres with a radius of 26 μm, not affecting the overall viscosity of the suspension. The PMMA domain was defined as an anisotropic material with data taken from the COMSOL database, i.e., a density of 1190 kg m^{-3}, Poisson ratio of 0.40 and a Young's modulus of $3 \times 10^9 \, (1 + i/400)$ Pa. The speeds of sound in water and in the particles were assumed as 1481 m s^{-1} and 2340 m s^{-1}, respectively. The contrast factor is defined as [24]:

$$\Phi_Y = \frac{\zeta + 2/3(\zeta - 1)}{1 + 2\zeta} - \frac{1}{3\zeta\xi^2} \qquad (32)$$

where $\zeta = \rho_s/\rho_l$ and $\xi = c_s/c_l$. The piezoelectric material is a lead zirconate titanate Pz26 transducer and the material properties were introduced using data supplied by the manufacturer (http://www.ferroperm-piezo.com). Finally, the mass fraction of particles was set to $x_p = 0.01$.

3. Results and discussion

As explained earlier in Section 2.4, the first modelling step allows calculating the pressure field, velocity and acceleration of the harmonic wave. Fig. 3 shows the pressure amplitudes for frequencies of 1.51, 1.705 and 2.48 MHz. The strong changes of the pressure amplitudes at different frequencies are caused by resonance. Operating the system at frequencies close to a resonant frequency will yield higher pressures. The maximum pressure amplitude throughout the ramping process was found at 1.51 MHz. Therefore, maximum acoustic forces are found at the lower end of ramping. These forces are drastically reduced at higher frequencies. The majority of applied frequencies reach pressure amplitudes in the range of 1×10^5–2×10^5 Pa, similar to the one at 1.705 MHz shown in Fig. 3. Some resonance frequencies, which yield pressure amplitudes much higher than the average, caused numerical instabilities during the frequency sweep. When stabilisation could not be achieved the specific frequency was skipped while the following frequency was then solved for an additional 0.1 s step.
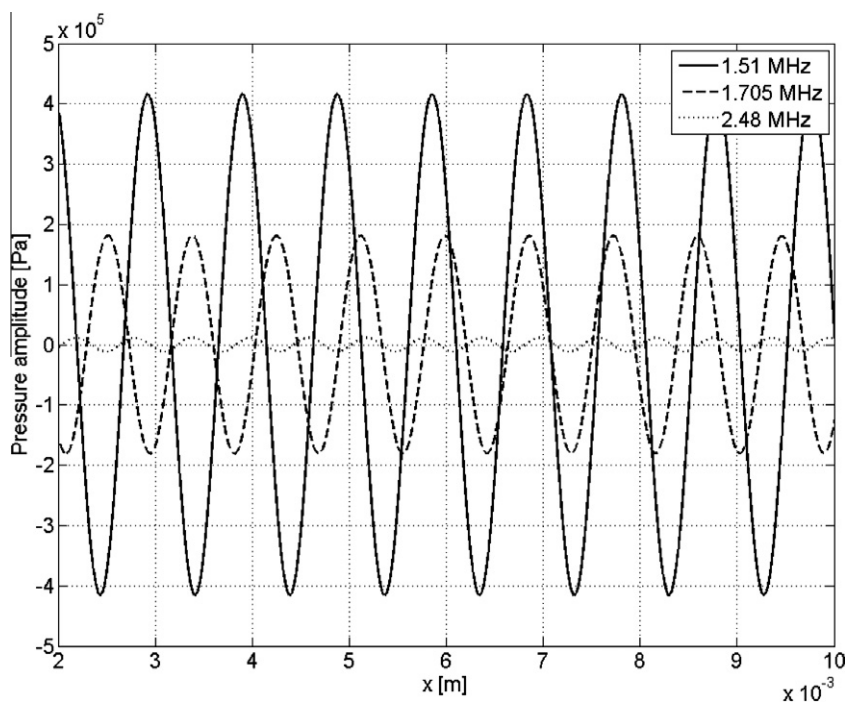
In the second step, predictions of the mean square fluctuation of the pressure $<p^2>$ and velocity $<v^2>$ are used to calculate the acoustic force potential given by Gork'ov's Eq. (5). Fig. 4 depicts a qualitative overview of the terms contributing to the acoustic radiation force. Values are plotted in a colour scale where red and blue colours represent maximum and minimum values, respectively. Fig. 4a illustrates the pressure amplitude on the full length of the geometry. Fig. 4b shows a magnified wavelength. Fig. 4c and d show the mean square fluctuation of the pressure amplitude $<p^2>$ and the mean square fluctuation of the velocity $<v^2>$ in the same magnified area. Both terms $<p^2>$ and $<v^2>$ are required to calculate Gork'ov's potential $<U_{Rad}>$ which is shown in Fig. 4e. The acoustic radiation force $<F_{Rad}>$ can finally be calculated with Eq. (4) and its norm is shown in Fig. 4f. At the pressure nodes, where pressure amplitude is zero, the acoustic force is also zero as it passes from positive to negative values when moving from left to right. This is represented by the black arrows showing how the acoustic force pushes the particles towards the nodes. The accumulation of particles on two distinct bands can be seen in Fig. 4g. The simulation shows that the acoustic force is strong enough to locate the particles on bands almost instantly. Only a single time step of 0.1 s was needed to accumulate particles on the nodes at 1.5 MHz. After that, the computation of ramping shows that the bands filled with particles moved following the movement of the nodal points.

The digital images at 0, 40 and 120 s shown in Möller et al. [21] and Dual et al. [22] were used for validating the model predictions. The images were imported by a purpose-developed function programmed in MATLAB™ (The Mathworks Inc., Natick, MA, USA) and converted from the original greyscale to a false colour intensity distribution, utilising the software's imaging toolbox capabilities, to visually observe the regions of maximum and minimum concentrations of particles. Since the modelled geometry consists of a thin cross section, a representative section of each image was selected through an additional feature in the MATLAB™ function. This cross section was taken close to the centre of the chamber where influences by the surrounding walls are minimal. In addition, an average value for the concentration of 15 pixels in
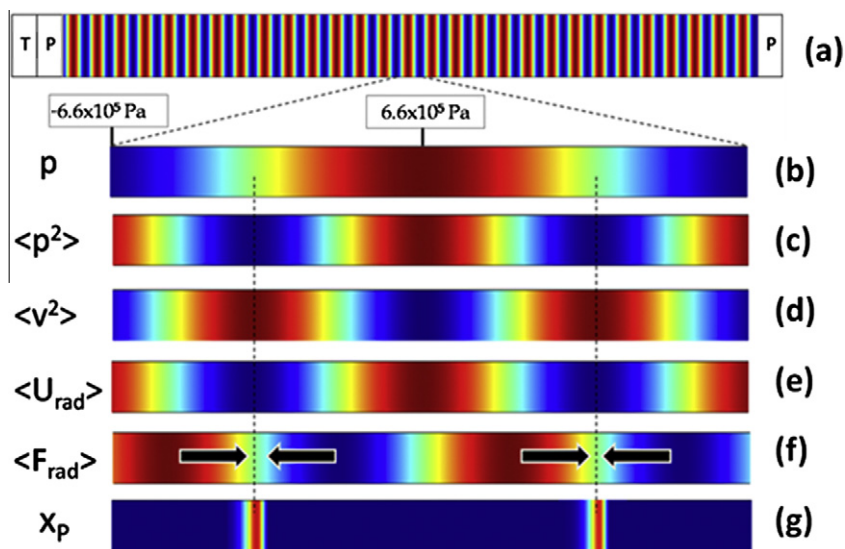

Fig. 3. Pressure amplitudes at three different frequencies.

Fig. 4. Qualitative overview of the different terms contributing to the Gork'ov equation at 1.54 MHz (blue colour indicating a minimum and red a maximum; arrows show the force vector of the acoustic radiation force; T = Transducer, P = PMMA). (For interpretation of the references to colour in this figure legend, the reader is referred to the web version of this article.)

y-coordinate, which equals to a distance of around 500 μm, was calculated to minimise artefacts which may have been caused by importing and converting the image. Furthermore, a threshold intensity was defined as a filter mechanism to get clear particle distributions, i.e., identifying the regions where particles were present from the remaining liquid domain. Finally, the values were normalised to allow for comparing them with the calculated mass fractions. The value for normalisation was taken from the 120 s image as it can be assumed that at this time the maximum concentration was reached in most bands.

Fig. 5 shows the initial condition (i.e., f = 1.5 MHz, with fully developed bands). The figure on the left shows the greyscale image, while the one on the right shows the converted false colour image. It can be seen that bands of particles are clearly formed, with the concentration of particles being higher in proximity to the transducer on the left side. At the bottom left of the image, particles are not visible around the circular shaped hole, which is the fluids and particle inlet. The figure also shows that some particles are

accumulated at the bottom. At the top, the bands are not as clearly separated from each other as in the middle part. Besides, the figure shows that the bands are not visible in some areas near the top boundary. These effects seen in close proximity to the walls are attributed to acoustic wave reflections. Therefore, and as indicated above, the black line in the false colour figure was selected to track the concentration of the bands in a position where there is minimal disturbance of the pressure field by the walls. Fig. 6 compares the mass fraction obtained from the experiments with that predicted by the simulation on the bands at time t = 0 s. Only peak concentrations and locations, where the threshold intensity is exceeded, are plotted to show the general trend of particles distributed within the separation chamber. Including the data from all areas throughout the chamber would not add any further beneficial information for validating the simulated scenario. The overall trend of the experimental data shows a maximum particle concentration at around 4–5 mm with a subsequent decrease, followed by an increase near the right hand side of the chamber. This trend is
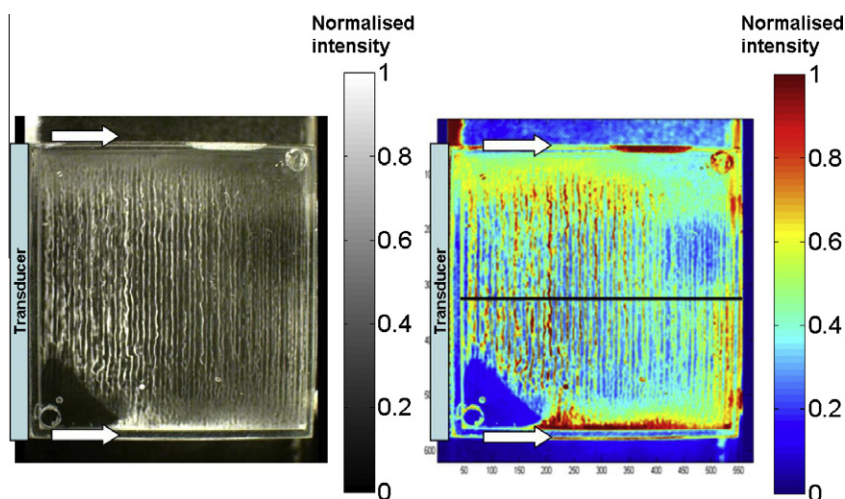

Fig. 5. Images for time t = 0 s in greyscale (left) and as false colour intensity distribution (right) with arrows indicating the movement direction of the bands and the black line indicating the points where the experimental data was extracted (Transducer on the left side of each image). (For interpretation of the references to colour in this figure legend, the reader is referred to the web version of this article.)
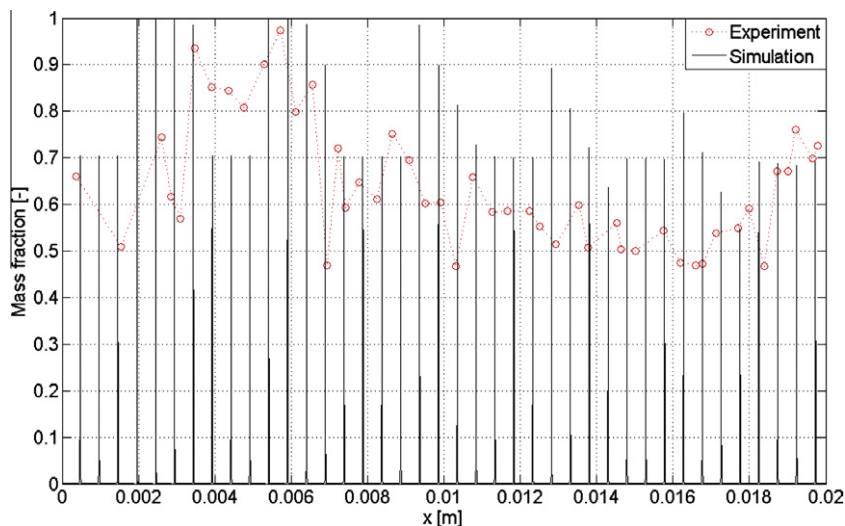
Fig. 6. Comparison of the initial condition for the simulation and experiment at time t = 0 s.
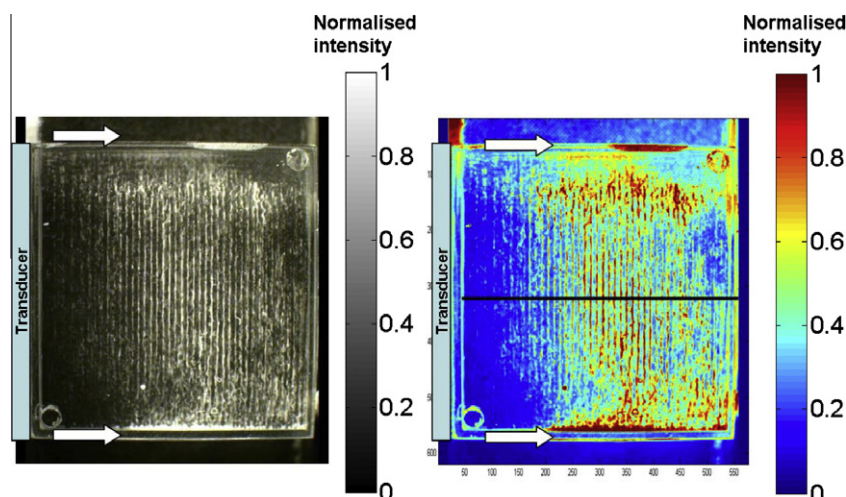

Fig. 7. Images at 40 s in greyscale (left) and as false colour intensity distribution (right) with arrows indicating the movement direction of the bands and the black line indicating the points where the experimental data was extracted (Transducer on the left side of each image). (For interpretation of the references to colour in this figure legend, the reader is referred to the web version of this article.)

also observed in the simulated scenario, although the predicted particle concentration is higher than that of the experiment.

Fig. 7 displays images at 40 s. It shows that in just 2 completed ramps from 1.5 to 2.5 MHz, most of the particles in close proximity to the transducer have migrated to the middle of the separation chamber. Additionally, the particles close to the bottom of the image, which were observed on the image at 0 s (c.f., Fig 5), are still accumulated at the bottom without further movement to the right. Particles along the black line clearly show a displacement of the bands towards the right hand side. Furthermore, particles at the top, which did not form clear bands on the previous pictures, are now well aligned within the bands. Fig. 8 shows the experimentally determined and calculated peak particle concentration (mass fraction) and location of the bands at 40 s. Peaks from Fig. 7 that are below the threshold setting are not plotted in Fig. 8. These peaks below the threshold are visible in Fig. 7 as light blue lines close to the transducer. Fig. 8 shows peaks of high concentration between 10 and 14 mm. After 14 mm the concentration within the bands decreases. The model followed the trend of the experimental data although the modelled concentrations are generally higher. This is because the acoustic force is higher than the

diffusive force except when the concentration approaches saturation. Hence, the mathematical model tends to over predict the maximum concentration of the bands. To correct this problem Eq. (23) was introduced aiming at balancing the acoustic force at high concentration of particles. The first visible band is around 7 mm for the experiment as well as the simulation. The strongest deviation between the experimental and modelled data is located on the left side where the concentration of particles is lower than the calculated concentration. Overall, the trend in the experimental data is in good agreement with the simulation also at the 40 s time step.

Fig. 9 shows the images at the final time step of 120 s. It can be seen that after 6 complete frequency sweeps most particles are located near the reflective wall on the right hand side. Fig. 10 displays the experimentally determined and predicted location of the bands, as well as the peak concentrations at 120 s. Again, the particles visible as light blue lines in the false-colour image were filtered out. The location is in good agreement with the experimental data, although the calculated concentration of the bands on the left is lower than that of the experiment. Fig. 11 displays the experimental and modelled location of bands for all three time steps, i.e.,
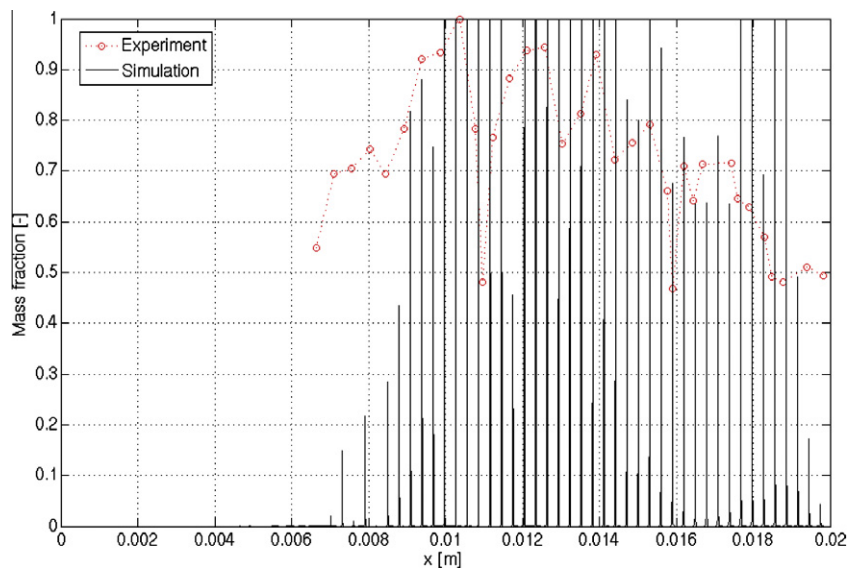
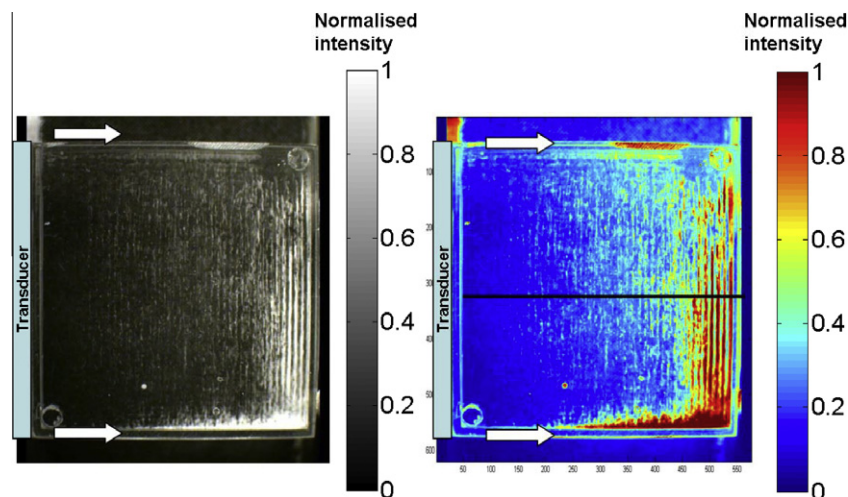**Fig. 8.** Comparison of simulation and experiment at 40 s.

Fig. 9. Images at 120 s in greyscale (left) and as false colour intensity distribution (right) with arrows indicating the movement direction of the bands and the black line indicating the points where the experimental data was extracted (Transducer on the left side of each image). (For interpretation of the references to colour in this figure legend, the reader is referred to the web version of this article.)

at the times 0, 40 and 120 s (or 0, 2 and 6 complete frequency sweeps). The figure shows an excellent agreement between predicted and experimentally determined data. It is concluded that while modelling the pressure fields may suffice to determine the nodal points where the particles bands are formed, only when solving the transient transport of concentrated species (c.f., Eq. (21)) it can be revealed how the particles get quickly concentrated at the nodes, thus, confirming the observed movement of the bands. Hence, the model is accurately describing the effect of the acoustic force on the particles as it shows how the acoustic force effectively moves and locates particles on the nodes.

Fig. 12 shows the trajectory of particles located on the first band on the left hand side. On the figure, displacement is referred as the distance between the wall on the transducer side and the first band of particles. As can be seen, a particle located in the first band experiences a steep increase in displacement of up to 3 mm for the first 6.2 s followed by a backward movement until the end of the first sweep cycle at 20 s, which was also observed in the experiments. A similar behaviour, where the displacement of particles increases

but then moves backwards, is also observed in the second frequency ramp (20–40 s). For subsequent frequency ramps after 40 s, only positive displacement of particles is observed. The figure also shows that the rate of increase of displacement steadily reduces for subsequent ramps after 40 s. It is expected that ramping beyond 120 s will lead to a steady state, where no net displacement will be observed. This is in agreement with Lipkens et al. [25], who developed an electroacoustic model to study the effect of frequency sweeping on the trajectory of particles. They found that the effect of ramping is to displace the particles away from the transducer towards the reflector. However, in the vicinity of the reflector, particles do not undergo a net translation but merely oscillate with the frequency sweeps. Hence, the model can be used to determine the number of ramps necessary to approach steady state where particles are located on bands on the close vicinity of the reflector, and where there is no net translation of particles as repeating frequency sweeps beyond this point does not lead to further separation but only oscillations on the trajectory of the particles.
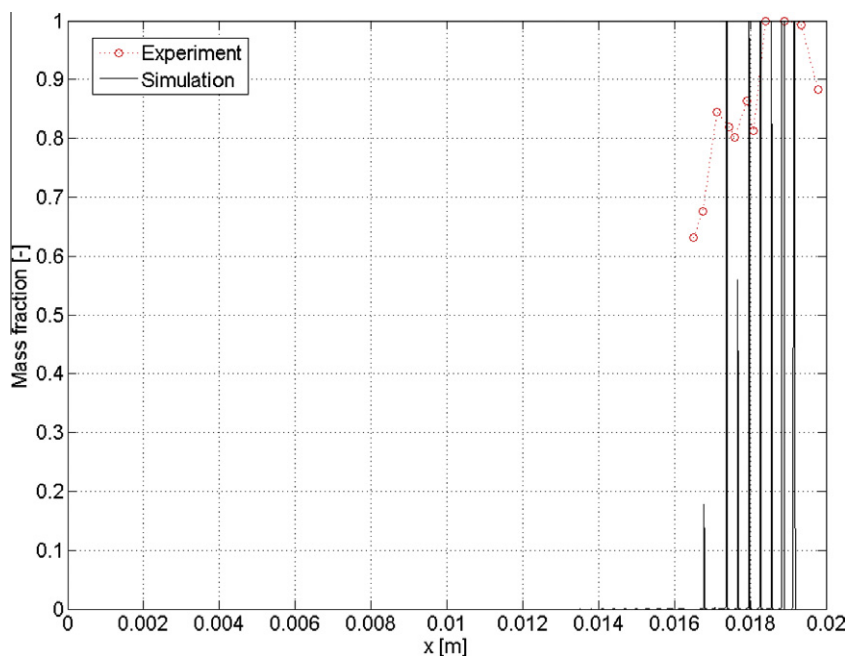
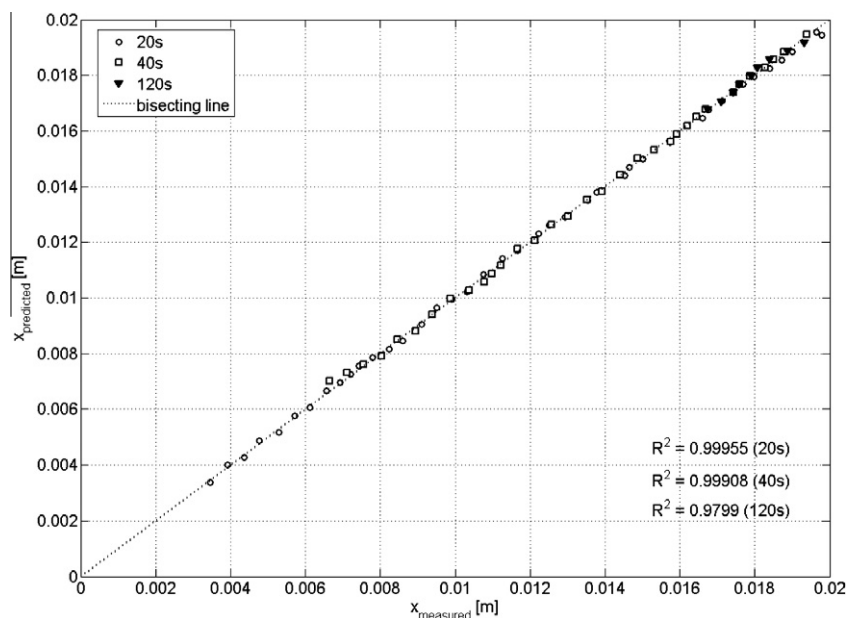**Fig. 10.** Comparison of simulation and experiment at 120 s.

Fig. 11. Comparison of predicted and measured location of particle bands.

The backward movement exhibited during the first 2 ramps can be explained with Fig. 13. As seen in Fig. 12, the displacement of a particle located on the first band reaches a maximum at 6.2 s. After that, particles start moving backwards until the end of the first ramp at 20 s. Fig. 13 displays the pressure waves from 6.2 to 6.7 s in steps of 0.1 s. At 6.2 s, a particle located on the grey circle is trapped in the pressure node of the wave illustrated with a black line. At 6.3 s (red line) the pressure node (black circle) has moved 0.5×10^{-4} m to the right of the grey circle. The calculated convective velocity for this time step is 10^{-4} m s^{-1} moving towards the black pressure node. At this velocity, a particle located at the grey circle would take 0.5 s to reach the black pressure node. Therefore,

in a time step of 0.1 s, there is not enough time for the particle to follow the pressure node. The particle will consequently lag behind the pressure node. The model shows that the particle will only travel 0.5×10^{-4} m between 6.2 and 6.7 s, approaching the black circle. At 6.7 s however, the closest pressure node of the standing wave (light blue line) will be located at the left hand side of the particle now located on the black circle. The vertical black line on the figure indicates the pressure antinode of the pressure wave at 6.7 s. That line demarcates the change on the direction of the acoustic force. The particle located on the black circle will, therefore, be moved towards the left hand side, explaining the backward movement. The backward movement for the second ramp can be
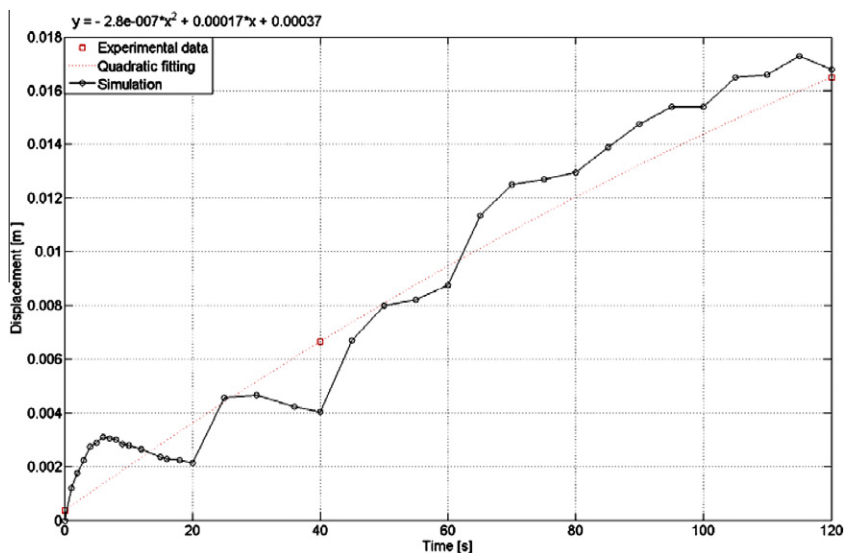
Fig. 12. Trajectory of the particles located on the band closest to the transducer during the ramping process (Displacement = distance between transducer and first band on the left hand side).
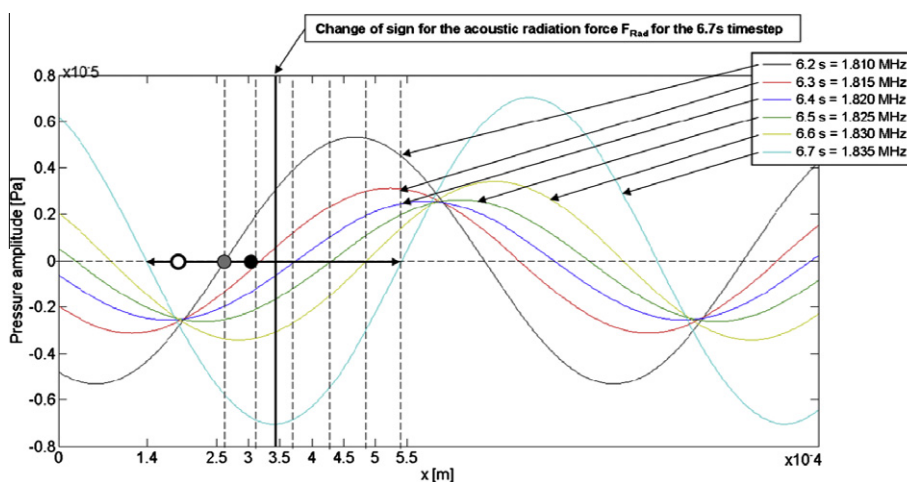

Fig. 13. Pressure amplitudes for 6.2–6.7 s, including the particle locations (6.2 s = grey circle, 6.6 s = black circle, 6.7 s = red circle) at the different time steps and the force vector for 6.7 s. (For interpretation of the references to colour in this figure legend, the reader is referred to the web version of this article.)

explained the same way. A possible solution for the initial backward movement would be to increase the acoustic force by increasing the voltage or by increasing the period of ramping. However, it should be noted that increasing the voltage higher than 7 V produce numerical instability because of the increase of the Péclet number.

4. Conclusion

The mass transport equation was modified to account for the effect of the acoustic forces on the concentration of particles. The proposed methodology allows modelling changes of concentration of particles on the physical domain. This approach is an alternative to modelling the movement of single particles, and it is, therefore, more suitable for larger scale applications where more pronounced gradients on the acoustic field and particle concentration are present. Besides, it is more efficient to model the changes on concentration than modelling the path of single particles at different initial positions to map the final concentrations as proposed by Townsend et al. [18]. The mass transport equation was successfully coupled with the time harmonic pressure acoustics model, allowing

the calculation of acoustic pressure, acoustic force and changes of the concentration of particles with time when sweeping the frequency following a sawtooth pattern. The model works well at low voltages and low initial concentration of particles, particularly, since higher voltages and higher concentrations cause high acoustic forces that leads to numerical instabilities. This is because the acoustic forces rapidly localize particles at the nodes while the calculated diffusivity approaches infinity as the concentration of particles approaches saturation (c.f., Eq. (23)). Eqs. (23) and (21) indicate that when the concentration of particles has reached saturation, the diffusive force will rise to balance the acoustic force so that no further increase of the concentration of particles can be achieved. In other words, once the bands are filled with particles, the diffusive and convective forces on Eq. (21) must be balanced:

$$-D\nabla(x_p\rho_T) - \frac{\nabla U_{Rad}}{C_D}(x_p\rho_T) = 0 \tag{33}$$

Introducing inconsistent stabilisation techniques allowed stabilising the model at low voltages and low concentration of particles. However, the model is unstable at higher voltages and higher particles concentrations.

The digital images revealed gradients of concentration on the y-direction towards the top and bottom of the geometry. This effect is attributed to reflections on the walls. The model did not take into account the influence of the PMMA bordering the top and bottom of the separation chamber due to the need of an extremely fine mesh that could not be solved with the available computational power. Overall, the predicted concentration of particle is in good agreement with the experimental data as it follows accurately the movement of the bands in the centre of the chamber. This is in spite of the simplifications of the model geometry and the need to run the model at lower voltage and lower initial concentration to achieve stabilisation. The model reveals a partial backward movement for the first 2 ramps. This was visually observed although it was not recorded on photographs. The model was used to explain that phenomenon in terms of the relationship between the acoustic force and the period of ramping. Hence, the simulation can give information to determine the period of ramping and voltage that reduce backward movement of particles. To the best of our knowledge, this is the first attempt to modify the mass transfer equation to determine the changes of concentration due to acoustic forces on the whole domain, which was successfully realised as shown by the good agreement with the data extracted from the digital photographs. It should be noted that there is still much to discover in the field of ultrasonic separation processes; particularly concerning simulations, where most of the modelling work has focused on determining the trajectory of single particles; but even more so in applications, where particles may agglomerate or even coalesce when approaching each other. This will lead to significant changes in the acoustic, drag and buoyancy forces, as well as the particles' diffusion behaviour.

References

[1] D.R. Garg, D.M. Ruthven, Te effect of the concentration dependence of diffusivity on zeolitic sorption curves, Chemical Engineering Science 27 (1972) 417–423.
[2] J. Nilsson et al., Review of cell and particle trapping in microfluidic systems, Analytica Chimica Acta 649 (2009) 141–157.
[3] G.R. Goddard et al., Analytical performance of an ultrasonic particle focusing flow cytometer, Analytical Chemistry 79 (2007) 8740–8746.
[4] T. Franke et al., Surface acoustic wave actuated cell sorting (SAWACS), Lab on a Chip 10 (2010) 789–794.
[5] T. Franke et al., Surface acoustic wave (SAW) directed droplet flow in microfluidics for PDMS devices, Lab on a Chip 18 (2009) 2625–2627.
[6] D. Foresti et al., Investigation of a line-focused acoustic levitation for contactless transport of particles, Journal of Applied Physics 109 (2011), http://dx.doi.org/10.1063/1.3571996.
[7] J.D.S. Gou, Y. Zhang, P. Hang, J. Zhang, A method and apparatus for demulsifying an oil–water emulsion via ultrasonic effect, 2005. WO/2005/030360.
[8] L.J. Stack et al., Factors influencing the ultrasonic separation of oil-in-water emulsions, Ultrasonics Sonochemistry 12 (2005) 153–160.
[9] M.V.Y. Maeda, C. Stavarach, K. Iwai, H. Oshige, Method for producing fatty alcohol ester, 2005, 6884900.
[10] P. Juliano et al., Enhanced creaming of milk fat globules in milk emulsions by the application of ultrasound and detection by means of optical methods, Ultrasonics Sonochemistry 18 (2011) 963–973.
[11] M. Gröschl, Ultrasonic separation of suspended particles – Part II: Design and operation of separation devices, Acoustica 84 (1998) 632–642.
[12] T.L. Tolt, D. Feke, Separation of dispersed phases from liquids in acoustically driven chambers, Chemical Engineering Science 48 (1993) 527–540.
[13] R. Barnkob et al., Measuring the local pressure amplitude in microchannel acoustophoresis, Lab on a Chip 10 (2010) 563–570.
[14] T. Laurell, F. Petersson, A. Nilsson, Chip integrated strategies for acoustic separation and manipulation of cells and particles, Chemical Society Reviews 36 (2007) 492–506.
[15] M. Hill, Y. Shen, J.J. Hawkes, Modelling of layered resonators for ultrasonic separation, Ultrasonics 40 (2002) 385–392.
[16] A. Neild, S. Oberti, J. Dual, Design, modeling and characterization of microfluidic devices for ultrasonic manipulation, Sensors and Actuators B: Chemical 121 (2007) 452–461.
[17] S. Oberti et al., Strategies for single particle manipulation using acoustic radiation forces and external tools, Physics Procedia 3 (2010) 255–262.
[18] R.J. Townsend et al., Modelling of particle paths passing through an ultrasonic standing wave, Ultrasonics 42 (2004) 319–324.
[19] H. Bruus, Theoretical Microfluidics, in: Oxford Master Series in Physics, Oxford University Press, 2007.
[20] L.P. Gor'kov, Forces acting on a small particle in an acoustic field within an ideal fluid, Soviet Physics, Doklady 6 (1962) 773.
[21] D. Möller, T. Schwarz, J. Dual, Flow-free transport of particles in a macro scale chamber, in: Ultrasound Standing Wave Action on Suspensions and Biosuspensions in Micro- and Macro Devices, International Centre for Mechanical Sciences, Udine–Italy, 2010.
[22] D. Jürg, H. Philipp, L. Ivo, M. Dirk, S. Thomas, W. Jingtao, Acoustofluidics 19: Ultrasonic microrobotics in cavities: devices and numerical simulation, Lab on a Chip 12 (2012) 4010–4021.
[23] D. Möller, T. Schwartz, J. Dual, Flow-free transport of particles in a macro scale chamber, in: Ultrasound Standing Wave Action on Suspensions and Biosuspensions in Micro- and Macro Devices, International Centre for Mechanical Sciences, Udine–Italy, 2010.
[24] K. Yosioka, Y. Kawasima, Acoustic radiation pressure on a compressible sphere, Acoustica 5 (1955) 167–173.
[25] B. Lipkens, M. Costol, E. Rietman, The effect of frequency sweeping and fluid flow on particle trajectories in ultrasonic standing waves, IEEE Sensors Journal 8 (2008) 667–677.